SCIENCE CHINA
Physics, Mechanics & Astronomy

•Article•

August 2022 Vol. 65 No. 8: 284212
https://doi.org/10.1007/s11433-022-1916-7

Dual-polarization two-dimensional valley photonic crystals

Xin-Tao He, Jian-Wei Liu, Fu-Long Shi, Ke Shen, Wen-Jie Chen, Xiao-Dong Chen*, and Jian-Wen Dong

School of Physics, State Key Laboratory of Optoelectronic Materials and Technologies, Sun Yat-sen University, Guangzhou 510275, China

Received January 26, 2022; accepted April 21, 2022; published online July 4, 2022

The recent realization of valley physics in photonic systems has enriched the topological phases of light with protected edge modes and shown applications in designing high-performance photonic devices. However, the widely reported valley Hall effect of light in two-dimensional systems is limited to one single polarization. Here, we present dual-polarization two-dimensional valley photonic crystals by simultaneously opening two frequency accidental degenerate Dirac cones. Two band gaps with different polarizations are characterized by opposite-valley Chern numbers, which are confirmed by the opposite-phase vortex distributions of bulk modes and opposite Berry curvatures. This situation results in the polarization-dependent refraction of bulk and edge modes, which locate in opposite valleys. The polarization-independent topological valley transport is also demonstrated. Our work shows the flexible control of light in topological photonic systems with a polarization degree of freedom and has applications in polarization multiplexing photonic devices.

topological photonics, valley photonic crystals, polarization

PACS number(s): 42.70.Qs, 42.25.Bs, 42.25.Ja

Citation: X.-T. He, J.-W. Liu, F.-L. Shi, K. Shen, W.-J. Chen, X.-D. Chen, and J.-W. Dong, Dual-polarization two-dimensional valley photonic crystals, Sci. China-Phys. Mech. Astron. **65**, 284212 (2022), https://doi.org/10.1007/s11433-022-1916-7

1 Introduction

The introduction of topology in photonic systems has attracted considerable attention not only for the elaborate topological phases of light but also for its practical applications in novel photonic devices [1-6]. The quantum Hall effect of light was realized in photonic crystals (PCs) by introducing external electric or magnetic fields to break the time-reversal symmetry (TRS) [7-15]. Based on the propagation of one-way edge modes along its boundary, robust photonic waveguides can be designed and demonstrated. Instead of breaking the TRS, the quantum spin-Hall effect of light has been achieved in different TRS-preserved systems, such as metamaterials, coupled ring optical waveguides, and PCs, with the careful construction of photonic pseudospins [16-27]. With decoupled photonic pseudospins, the topologically protected optical propagation of pseudospin states was demonstrated, and photonic applications, such as high-performance topological lasers, were shown. Recently, the valley Hall effect of light has been realized by introducing the binary valley degree of freedom into photonic systems [28-38]. With the preservation of the TRS, the valley Hall effect of light in two-dimensional (2D) PCs, whose band gaps are characterized by nonzero valley Chern numbers, can be achieved. Such nontrivial band gaps can be realized in a triangular-lattice PC with broken mirror symmetry [28] or in a honeycomb-lattice PC with broken spatial inversion symmetry [30]. Furthermore, valley-dependent edge modes are found by constructing the domain wall using two PCs with opposite-valley Chern numbers. Under the suppression of

*Corresponding author (email: chenxd67@mail.sysu.edu.cn)

intervalley scattering between valley-dependent edge modes, the topological valley transport has shown prospects in the realization of photonic waveguides, splitters, and ring resonators [39-48].

The valley Hall effect of light is commonly realized in 2D photonic systems because it has sufficient degrees of freedom to control the flow of light and is compatible with semiconductor materials to realize nanophotonic devices. For electromagnetic waves that propagate within the xy plane, the eigenmodes of a 2D photonic system can be classified into two decoupled modes (or polarizations), namely, the transverse-electric (TE) modes with nonvanishing E_x, E_y, and H_z components and transverse-magnetic (TM) modes with nonvanishing H_x, H_y, and E_z components. However, the most reported valley Hall effect of light in 2D PCs is limited to one single polarization, hindering its applications in polarization multiplexing photonic devices. In this work, we present the polarization-valley Hall effect of light in a 2D triangular-lattice PC. The accidental degeneracy of frequencies of Dirac cones with TE and TM polarizations, i.e., accidental dual-polarization Dirac cones, are realized by changing the filling ratio of metallic rods in a dielectric background. The accidental dual-polarization Dirac cones play important roles in the realization of band gaps for both polarizations. The resultant TE- and TM-polarized band gaps with opposite-valley Chern numbers lead to the polarization-valley Hall effect of light. Two key phenomena of the polarization-valley Hall effect of light, i.e., polarization-dependent refraction of bulk modes into the homogeneous medium and polarization-dependent edge modes at the domain wall, are demonstrated. Aside from the polarization-dependent phenomena, the polarization-independent topological valley transport is also presented.

2 Results and discussion

2.1 Accidental dual-polarization Dirac cones

In this study, we consider a 2D triangular lattice of PCs with the lattice constant of a (Figure 1(a)). The unit cell consists of an equilateral triangular rod in the dielectric background, with a relative permittivity of $\varepsilon_r = 2.25$. The triangular rod is considered a perfect electric conductor that can be achieved by metals in the microwave regime. The side length of the triangular rod is s_0, which controls the filling ratio of the central rod (or the outer dielectric background). The angle between the tip of the rod and the positive x-direction is denoted by θ. Without loss of generality, we first consider the PC with $s_0 = 0.8a$ and $\theta = 0°$ (left inset in Figure 1(c)) and numerically simulate its bulk band dispersions using a finite element method (COMSOL Multiphysics^{TM}. COMSOL AB, Stockholm, Sweden). Figure 1(c) shows the band dispersions of the TE and TM bulk modes in red and blue, respectively. TM modes have a nonzero cutoff frequency $f = 0.743c/a$, below which there is an absence of passing bands, while TE modes start from the zero frequency. This finding is in agreement with previously reported results that discuss 2D metallic PCs [49-51]. Within the frequency range from 0 to c/a, six bulk bands for TE modes and two bulk bands for TM modes exist. Particularly, the first and second TE-polarized bands linearly cross near the corner of the Brillouin zone, i.e., the K point. The crossing point of the band dispersion at the K point is called the Dirac point, and band dispersions around lead to the Dirac cone. Moreover, Dirac cones are found in the fourth and fifth TE-polarized bands and first and second TM-polarized bands. The existence of Dirac cones around the K point has been widely discussed in 2D triangular or honeycomb crystals whose point group symmetry is favored in the realization of Dirac cones [38,52-54]. Although Dirac cones are found for TE and TM polarizations, their frequencies are different, i.e., $f_{TE,1} \neq f_{TM,1}$ and $f_{TE,2} \neq f_{TM,1}$, as the electromagnetic duality symmetry of the 2D PC is broken (i.e., ε/μ is not a constant over the whole real space). However, by changing the filling ratio of metallic rods, the frequencies of Dirac points for both polarizations can accidentally degenerate at a specific filling ratio, and accidental dual-polarization Dirac cones can be achieved. To examine this condition, we enlarge the side length of metallic rods and plot the evolution of the frequencies of the second-lowest TE Dirac modes (i.e., $f_{TE,2}$) and first-lowest TM Dirac modes (i.e., $f_{TM,1}$) in red and blue, respectively (Figure 1(b)). As a function of s_0, an accidental degeneracy occurs between TE- and TM-polarized Dirac frequencies, i.e., $f_{TE,2} = f_{TM,1}$, which implies the realization of dual-polarization Dirac cones. For further details, Figure 1(d) shows the band dispersions of TE and TM bulk modes for the PC with $s_0 = 0.845a$ and $\theta = 0°$. Only band dispersions within the normalized frequency range from 0.6 to 1 are shown here for brevity. Clearly, at a frequency of $0.844c/a$, doubly degenerate bulk modes are found for TE and TM polarizations. Near the frequency of $0.844c/a$, linear band dispersions are found around the K point for both polarizations. This result proves the realization of accidental dual-polarization Dirac cones by changing the filling ratio of metallic rods. In addition, both Dirac cones are frequency isolated. That is, no other bulk modes exist at the Dirac frequency except the bulk modes at the K point. Furthermore, these accidental dual-polarization Dirac cones serve as good candidates for achieving complete band gaps and polarization-valley Hall effect of light by opening the Dirac cones, which will be discussed in the next section. In particular, they are much less robust than single-polarization Dirac cones that are not accidental, as the accidental dual-polarization Dirac cones are sensitive to the changes in the side length s_0. Essentially, the realization of accidental Dirac cones is a good starting point but not the necessary condition to achieve dual-polarization-

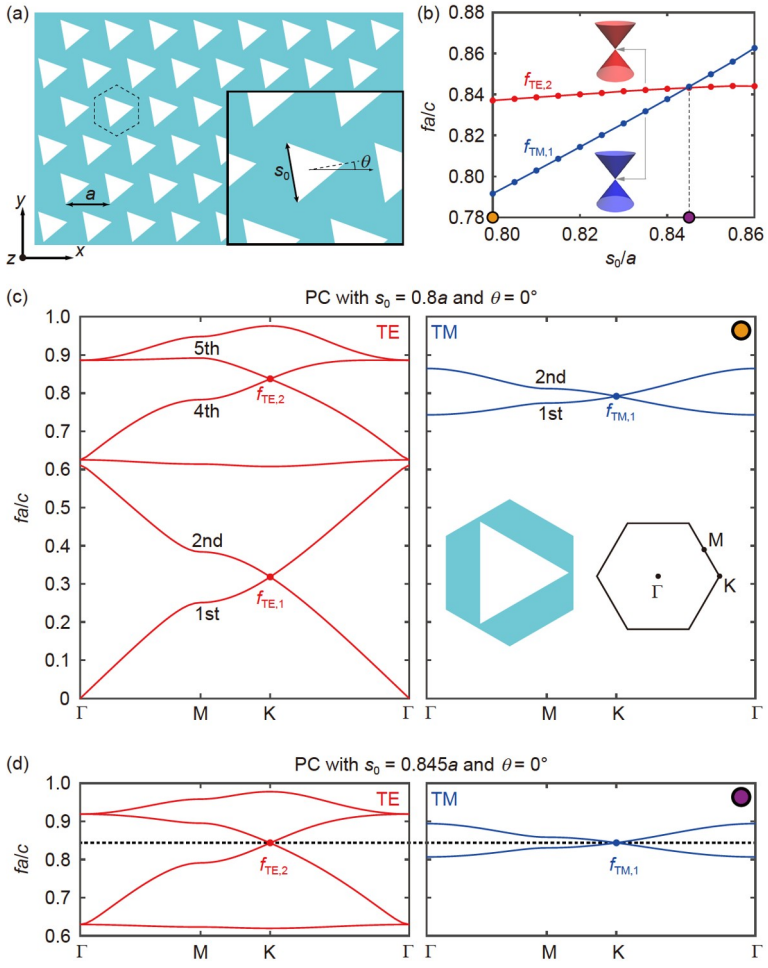

Figure 1 (Color online) Dual-polarization Dirac cones in the two-dimensional photonic crystal (PC). (a) Schematic of the PC consisting of periodic equilateral triangular metallic rods (white) in the dielectric background (cyan) with a relative permittivity of $\varepsilon_r = 2.25$. The lattice constant is a. The enlarged inset shows that the side length of the metallic rod is s_0, and the angle between the tip of the metallic rod and the positive x-direction is θ. Here, the positive θ is obtained when the rod is rotated anti-clockwise around its center. (b) Evolution of the frequencies of the fourth- and fifth-lowest TE modes and the first- and second-lowest TM modes at the K point are shown in red and blue, respectively. The accidental frequency degeneracy of the TE- and TM-polarized Dirac cones (i.e., $f_{TE,2} = f_{TM,1}$) is achieved at the PC with $s_0 = 0.845a$. Two representative PCs presented in (c) and (d) are labeled by the orange and purple dots. (c) Band dispersions of TE and TM bulk modes of the PC with $s_0 = 0.8a$ and $\theta = 0$. Around the K point, Dirac cones are found between the first and second TE bands, fourth and fifth TE bands, and first and second TM bands. The schematics of the unit cell and first Brillouin zone are shown as insets. (d) Band dispersions of the TE and TM bulk modes of the PC with $s_0 = 0.845a$ and $\theta = 0$. The accidental dual-polarization Dirac cones are found. Here, only band dispersions within the normalized frequency range from 0.6 to 1 are shown.

valley PCs. As presented in Appendix A of Supplementary Materials, one can also obtain dual-polarization 2D valley PCs without the accidental Dirac cones, as long as the dual-polarization topological nontrivial band gaps can partially share the same frequency range.

2.2 Polarization-valley Hall effect of light

The realization of accidental dual-polarization Dirac cones is a good starting point in achieving the polarization-valley Hall effect of light in PCs by opening the gapless Dirac cones. To examine this, we note that the existence of the gapless Dirac cone around the zone corner is protected under the combination of the TRS and mirror symmetry. Therefore, to open the Dirac cone and obtain a complete band gap, we consider PCs with broken mirror symmetry, which are easy to realize. By rotating the central metallic rod around the origin with an angle of θ, the mirror symmetry is broken, and the degenerate bulk Dirac modes at the K point are split. As a function of θ, Figure 2(a) shows the frequency spectra of the fourth and fifth TE-polarized bulk modes at the K point and Figure 2(b) for the first and second TM-polarized bulk modes at the K point. When θ is nonzero, the degenerate Dirac modes split and band gaps are obtained for both polarizations. Although both band gaps are omnidirectional, they are characterized by different valley Chern numbers, which can be inspected by the eigen fields of bulk modes just below the band gap. To examine this, the amplitude of H_z fields (i.e., $|H_z|$) and power fluxes of two TE-polarized bulk modes are shown in the inset of Figure 2(a). Both modes

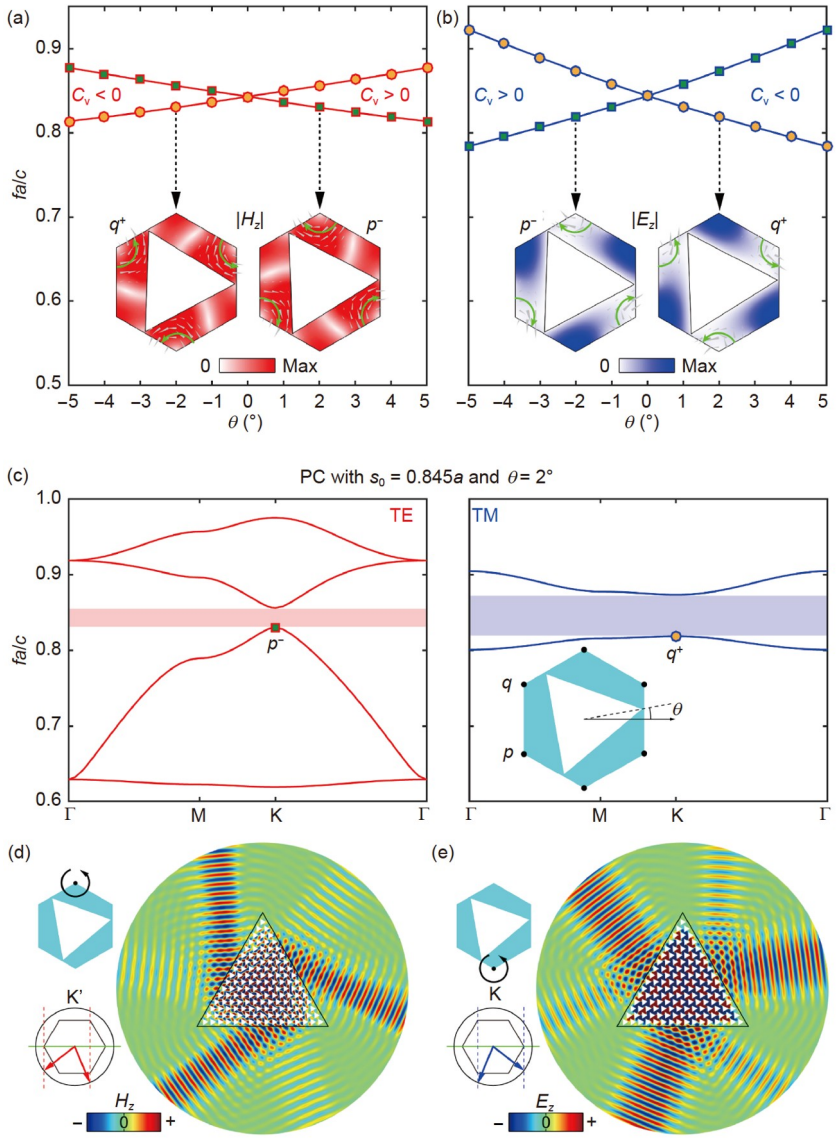

Figure 2 (Color online) Polarization-valley Hall effect. Evolution of bulk modes at the K point as a function of θ for (a) TE polarization and (b) TM polarization. The valley Chern number is given for each band gap, and the topological phase transition happens at $\theta = 0°$, where the closing of both gaps happens. The eigen fields and power fluxes of the representative bulk modes (p^- and q^+ modes) are shown in insets. (c) TE- and TM-polarized bulk bands of the PC with $\theta = 2°$. Band gaps for TE and TM polarizations are shaded in red and blue, respectively. The inset shows the schematic of the unit cell. The angle between the tip of the metallic rod and the positive x-direction is marked by θ. Here, the positive θ is obtained when the rod is rotated anti-clockwise around its center. The mirror symmetry along the x-axis is broken when θ is nonzero. Polarization-dependent refraction of bulk modes of (d) TE polarization and (e) TM polarization. The schematic of the excitation with the chiral source and the k-space analysis of the refraction of bulk modes are shown in the left panel. The outcoupled fields of the excited bulk modes of the PC into the air are shown in the right panel.

have their vanishing H_z fields at the triangular-lattice corner p or q, and chiral power fluxes are observed around these corners. Here, the mode with an anti-clockwise power flux around the triangular-lattice corner q is labeled as the q^+ mode. On the contrary, the mode with a clockwise power flux vortex around the triangular-lattice corner p is labeled as the p^- mode. With the increasing θ, the two modes come closer, meet each other, and separate apart once again. Along with this mode exchange, a topological phase transition happens, and the valley Chern number changes from negative to positive (see Appendix B of Supplementary Materials for the numerical calculation of Berry curvatures and valley Chern numbers). A similar topological phase transition is also found in the TM-polarized bulk modes, but the valley Chern number changes from positive to negative because the lowest bulk modes changes from the p^- mode to the q^+ mode. This finding indicates that the TE- and TM-polarized band gaps are characterized by opposite-valley Chern numbers, i.e., the polarization-valley Hall effect.

The polarization-valley Hall effect of light can be inspected from the polarization-dependent refraction of bulk modes into the homogeneous medium. To be concrete, we

consider a PC with $s_0 = 0.845a$ and $\theta = 2°$ and plot its bulk dispersions in Figure 2(c). A band gap ranging from $0.83c/a$ to $0.856c/a$ ($0.819c/a$ to $0.874c/a$) is found for the TE (TM) polarization, shaded in red (blue). Below the band gap, the fourth TE-polarized bulk mode has a clockwise power flux vortex of H_z fields at hexagonal unit cell corners p, i.e., the p^- state (right inset of Figure 2(a)). On the contrary, the first TM-polarized bulk mode has an anti-clockwise power flux vortex of E_z fields at hexagonal unit cell corners q, i.e., the q^+ state (right inset of Figure 2(b)). As bulk modes below the band gap with different polarizations have contrasting field distributions, the TE gap is characterized by the valley Chern number of $C_v > 0$ and TM gap by $C_v < 0$, indicating that their valley Chern numbers are different. This finding indicates that bulk modes in opposite valleys can be selectively excited using a chiral source with the same phase vortex. Here, we consider the triangle-shaped PC whose three outer boundaries are along the ΓK direction and it is surrounded by the air (Figure 2(d) and (e)). Chiral sources with an anti-clockwise decreasing phase vortex are placed at the corners of the unit cell [27,38], and their operating frequencies are set to be $0.819c/a$. In particular, to excite bulk modes with different polarizations, the source component should be changed to H_z for the TE polarization and to E_z for the TM polarization. The corresponding bulk modes in different valleys will be excited only when their phase chirality matches the chirality of the source [30,55]. For example, when the source with an anti-clockwise decreasing phase vortex is put at the unit cell corner p, bulk modes at the K′ valley are excited (left top panel of Figure 2(d)). The refraction of bulk modes into the air can be analyzed by the phase-matching condition at the interface between the PC and air. Here, we take the refraction of bulk modes at the interface along the x direction as an example (left panel in Figure 2(d)). The outer black circle outlines the dispersion of light at the frequency of $f = 0.819c/a$ in the air, and the inner hexagon marks the first Brillouin zone of the triangular lattice of the PC. For the bulk modes and refracted light beams, their wave vectors should be equal or differ by the integer multiple of the reciprocal lattice vector along the x direction, i.e., $\mathbf{k}_{\mathrm{bulk},x} = \mathbf{k}_{\mathrm{air},x} \pm 2\pi m / a$, where m is an integer [28,31]. As a result, there will be two refracted light beams whose directions are given by two red arrows in the left bottom panel of Figure 2(d). Directions of simulated refracted light beams are in good agreement with those of the results based on the k-space analysis (right panel in Figure 2(d)). Conversely, when the source is changed to be placed at unit cell corners q, bulk modes at the K valley are excited (left panel in Figure 2(e)). As bulk modes at opposite valleys are excited, the directions of refracted light will be switched, which is confirmed by our numerical results shown in the right panel of Figure 2(e).

The polarization-valley Hall effect can also be inspected from the polarization-dependent edge modes of the domain wall. To examine this, we consider the domain wall between the PC with $\theta = -2°$ at the top and the PC with $\theta = 2°$ at the bottom (Figure 3(a)). The valley Chern numbers of the TE and TM gaps are $C_v > 0$ and $C_v < 0$ for the PC with $\theta = 2°$, while the valley Chern numbers of the TE and TM gaps of the PC with $\theta = -2°$ are reversed and changed to $C_v < 0$ and $C_v > 0$. Therefore, the two PCs are topologically distinct, and edge modes should be found at the domain wall between them. Figure 3(c) and (d) show the dispersions of the corresponding edge modes (marked in red or blue). Based on the difference of the valley index at the K valley crossing the domain wall, the group velocity direction of edge modes for the TE (TM) polarization at the K valley is positive (negative). Figure 3(b) plots the eigen fields of the represented valley edge modes with TE polarization (left) and TM polarization (right). Due to a larger band gap, the TM-polarized edge mode has stronger field confinement than the TE-polarized edge mode. Although valley-dependent edge modes are found in both polarizations, their group velocity directions are polarization-dependent. This is the manifestation of the polarization-valley Hall effect and can be used to achieve the polarization-dependent refraction of edge modes into the air. To examine this, we place the source at the left part of the domain wall, and rightward-propagating edge modes are excited (Figure 3(e) and (f)). The interface between the PC with the domain wall and air is set to be along the ΓK direction, and this interface morphology is used to suppress the intervalley scattering [28,31,56]. The operating frequency of sources is set to $0.845c/a$ at which edge modes of both polarizations can be found. When TE-polarized light is incident, the rightward-propagating edge modes at the K valley will be excited (left top panel of Figure 3(e)). Once again, based on the phase-matching condition, their refraction into the air can be theoretically obtained through the k-space analysis (left bottom panel of Figure 3(e)) and numerically confirmed with the outcoupled H_z field distributions (right panel of Figure 3(e)). Two refracted light beams (one pointing almost along the $-y$ direction and one almost along the $+x$ direction) are found, and their directions are in good agreement with those that are predicted in theory. By contrast, when the polarization of the incident light is switched from the TE to TM polarizations, rightward-propagating edge modes at the K′ valley (instead of the K valley) are excited (left top panel of Figure 3(f)), and their refracted direction into the air is altered (left bottom panel of Figure 3(f)). The change in the refraction direction of outcoupled light beams is also confirmed by our numerical results, in which two light beams with different propagating directions are found (right panel of Figure 3(f)). Therefore, polarization-dependent refraction is demonstrated, which serves as potential applications in the design of polarization multiplexing photonic devices, such as polarization beam splitters.

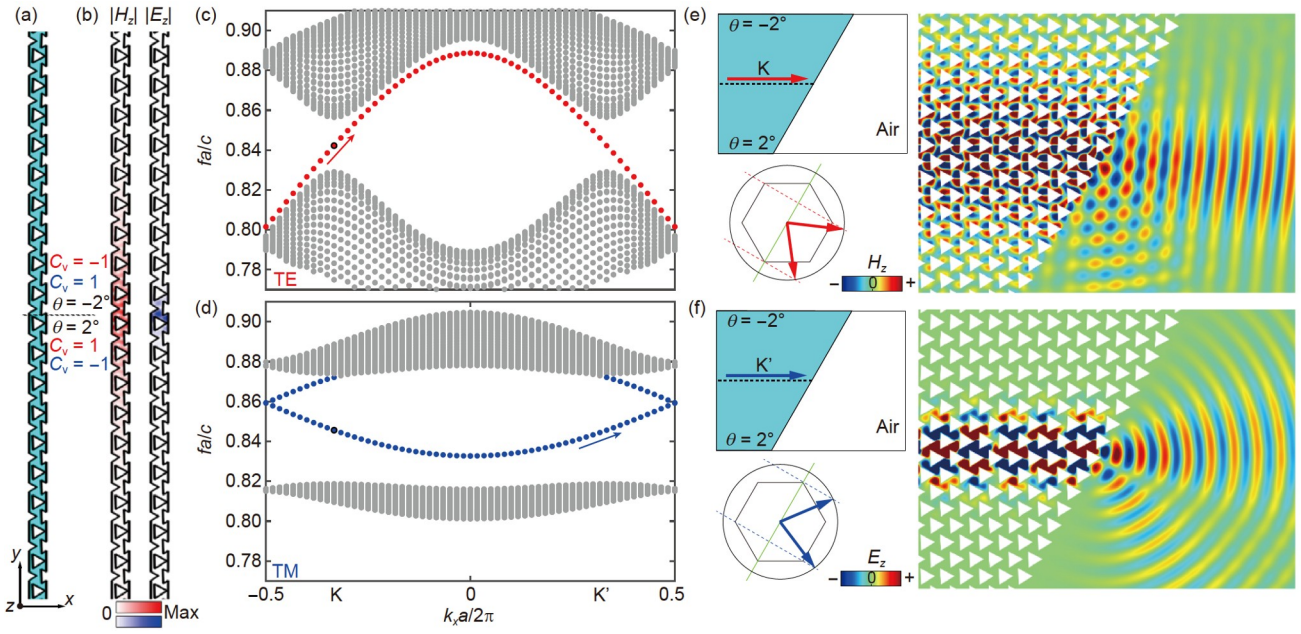

Figure 3 (Color online) Polarization-dependent edge modes. (a) Schematics of the domain wall between the PC with $\theta = -2°$ at the top and PC with $\theta = 2°$ at the bottom. (b) Eigen fields of the represented edge modes for the TE polarization (left) and TM polarization (right). (c), (d) Band dispersions of the edge modes of the domain wall. Valley-dependent edge modes are found at both band gaps, and their group velocities are determined by the valley Chern number difference across the domain wall. The representative edge modes, whose eigen fields are presented in (b), are outlined in black. (e), (f) Polarization-dependent refraction of rightward-propagating edge modes. The schematic of the excitation of edge modes in the opposite valley and the *k*-space analysis of the refraction of edge modes are shown in the left panel. The outcoupled fields of the excited edge modes into the air are shown in the right panel.

2.3 Polarization-independent topological valley transport

Aside from the two key polarization-dependent phenomena discussed in the above section, polarization-independent light propagation can also be achieved in the proposed dual-polarization 2D valley PC. For example, although the above-discussed edge modes are polarization-dependent, the robust transport of edge modes is polarization independent, and it can be achieved under the suppression of the intervalley scattering. To demonstrate the robustness of edge modes, we design three different waveguides, i.e., without the domain wall (left panel), with the flat domain wall (middle panel), and with the Z-shape domain wall (right panel), as schematically shown in Figure 4(a). For the latter two waveguides, the domain wall is constructed by the PC with $\theta = 2°$ at the bottom and the PC with $\theta = -2°$ at the top, while the first waveguide only consists of a PC with $\theta = 2°$. The incident source with the TE or TM polarization is placed on the left side of the waveguide, and a detector is placed on the right side to measure the transmittance. Figure 4(b) and (c) plot the transmission spectra of the TE and TM modes along the three waveguides. The transmittances of the three different waveguides are marked in gray, green, and pink, respectively. The low transmittance of the first waveguide means that there are no bulk modes, and the low-transmittance frequency ranges correspond to the frequency band gaps of the PC. When the operating frequency of the incident source is inside that of valley-dependent edge modes (shaded in red or blue), the excited edge modes are backscattering suppressed even when they meet the sharp corners. This result is confirmed by the same transmittance of the Z-shape bend as that of the flat channel. Of note, the transmittance shows a plateau feature in the frequency from $0.83c/a$ to $0.86c/a$ for the TE case, while peaks and dips are observed in the corresponding frequency region for the TM case. This is because the bulk band dispersions of TM modes deviate from the effective Dirac Hamiltonian. Backscattered waves are induced when the excited TM-polarized edge modes encounter the right output port. The interference between the forward and backward waves causes the peaks and dips in the corresponding frequency region for the transmittance of TM-polarized edge modes. The field patterns of the excited TE- and TM-polarized edge modes at the frequency of $0.845c/a$ are given in Figure 4(d) and (e). The field patterns show that both edge modes smoothly pass through two sharp corners, proving the polarization-independent topological valley transport. Therefore, by manipulating the polarization degree of freedom, enhancing the capacity of data multiplexing in topological waveguides is promising.

3 Conclusions

In this study, we realize accidental dual-polarization Dirac cones in PCs by tuning the filling ratio of the metallic rod within the dielectric background. The polarization-valley

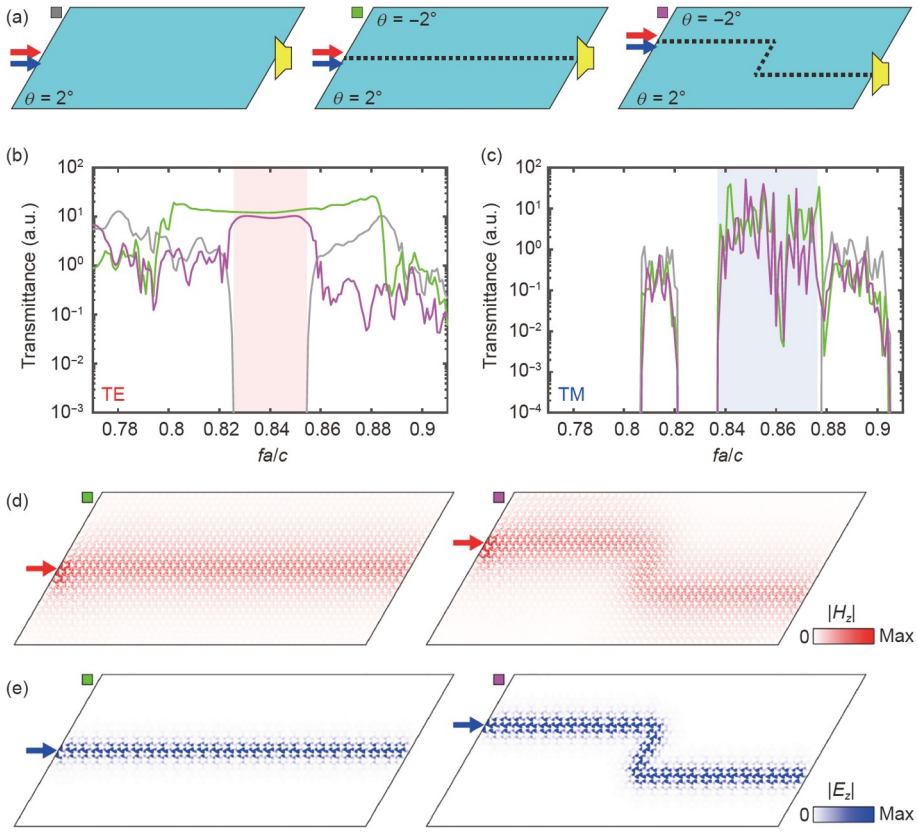

Figure 4 (Color online) Polarization-independent topological valley transport. (a) Schematics of three waveguides: without the domain wall (left), with the flat domain wall (middle), and with the Z-shape domain wall (right). TE- or TM-polarized light is incident from the left, and the transmission is measured at the right output. Transmission spectra for three waveguides when (b) the TE-polarized or (c) TM-polarized incident light is considered. The robust transport of edge modes can be achieved for both polarizations, proving the polarization-independent topological valley transport. Eigen fields of transmitted electromagnetic waves with the frequency of 0.845c/a for (d) TE and (e) TM polarizations.

Hall effect of light is achieved by opening the accidental dual-polarization Dirac cones in a simultaneous manner. The polarization-dependent refractions of bulk and edge modes in opposite valleys are demonstrated. In addition, the polarization-independent topological valley transport is presented. The introduction of polarization degrees of freedom into valley photonic systems provides an opportunity for the flexible control of the flow of light, and it has potential applications in the design of polarization multiplexing photonic devices. The simulation models are presented in Appendix C of Supplementary Materials.

We consider ideal 2D PCs, in which TE and TM modes are entirely decoupled. For a practical multilayer system, TE and TM modes are coupled when the mirror symmetry is broken along the z direction. Consequently, TE and TM edge modes in Figure 3(c) and (d) will not be gapless within each valley, and a partial gap will appear. However, topologically protected vector edge states are still found in dual-polarization-valley PC slabs [57]. Some other interesting phenomena may happen when TE and TM modes are coupled. For example, higher-order topological physics and related corner states can be explored within the band gap when edge modes are coupled [58,59]. For another example, the spin-Hall effect of light can be explored by constructing the photonic pseudospin with coupled TE and TM modes [60,61]. Conversely, the mirror symmetry of PCs along the x direction is broken by introducing a nonzero rotation angle of the central metallic rod. This case can also be achieved by changing the relative permittivity of the dielectric background. One example is presented in Appendix D of Supplementary Materials.

This work was supported by the National Natural Science Foundation of China (Grant Nos. 12074443, 62035016, and 11904421), Guangdong Basic and Applied Basic Research Foundation (Grant No. 2019B151502036), Guangzhou Science, Technology and Innovation Commission (Grant Nos. 201904010223, 202002030322, and 202102020693), and the Fundamental Research Funds for the Central Universities (Grant Nos. 20lgzd29, 20lgjc05, and 2021qntd27).

Supporting Information

The supporting information is available online at http://phys.scichina.com and https://link.springer.com. The supporting materials are published as submitted, without typesetting or editing. The responsibility for scientific accuracy and content remains entirely with the authors.

1 L. Lu, J. D. Joannopoulos, and M. Soljačić, Nat. Photon. **8**, 821 (2014), arXiv: 1408.6730.
2 Y. Wu, C. Li, X. Hu, Y. Ao, Y. Zhao, and Q. Gong, Adv. Opt. Mater. **5**, 1700357 (2017).
3 T. Ozawa, H. M. Price, A. Amo, N. Goldman, M. Hafezi, L. Lu, M. C. Rechtsman, D. Schuster, J. Simon, O. Zilberberg, and I. Carusotto, Rev. Mod. Phys. **91**, 015006 (2019), arXiv: 1802.04173.
4 M. Kim, Z. Jacob, and J. Rho, Light Sci. Appl. **9**, 130 (2020).
5 S. Xia, D. Song, N. Wang, X. Liu, J. Ma, L. Tang, H. Buljan, and Z. Chen, Opt. Mater. Express **11**, 1292 (2021), arXiv: 2103.16147.
6 G. J. Tang, X. T. He, F. L. Shi, J. W. Liu, X. D. Chen, and J. W. Dong, Laser Photon. Rev. **16**, 2100300 (2022), arXiv: 2201.06294.
7 F. D. M. Haldane, and S. Raghu, Phys. Rev. Lett. **100**, 013904 (2008), arXiv: cond-mat/0503588.
8 Z. Wang, Y. D. Chong, J. D. Joannopoulos, and M. Soljacić, Phys. Rev. Lett. **100**, 013905 (2008), arXiv: 0712.1776.
9 X. Ao, Z. Lin, and C. T. Chan, Phys. Rev. B **80**, 033105 (2009).
10 Y. Poo, R. X. Wu, Z. Lin, Y. Yang, and C. T. Chan, Phys. Rev. Lett. **106**, 093903 (2011).
11 T. Ochiai, Phys. Rev. B **86**, 075152 (2012).
12 S. A. Skirlo, L. Lu, Y. Igarashi, Q. Yan, J. Joannopoulos, and M. Soljačić, Phys. Rev. Lett. **115**, 253901 (2015), arXiv: 1504.04399.
13 B. Bahari, A. Ndao, F. Vallini, A. El Amili, Y. Fainman, and B. Kanté, Science **358**, 636 (2017).
14 M. Wang, R. Y. Zhang, L. Zhang, D. Wang, Q. Guo, Z. Q. Zhang, and C. T. Chan, Phys. Rev. Lett. **126**, 067401 (2021), arXiv: 2009.03065.
15 Z. G. Chen, J. Mei, X. C. Sun, X. Zhang, J. Zhao, and Y. Wu, Phys. Rev. A **95**, 043827 (2017).
16 W. Gao, M. Lawrence, B. Yang, F. Liu, F. Fang, B. Béri, J. Li, and S. Zhang, Phys. Rev. Lett. **114**, 037402 (2015), arXiv: 1401.5448.
17 Y. Yang, Z. Gao, H. Xue, L. Zhang, M. He, Z. Yang, R. Singh, Y. Chong, B. Zhang, and H. Chen, Nature **565**, 622 (2019), arXiv: 1804.03595.
18 M. Hafezi, E. A. Demler, M. D. Lukin, and J. M. Taylor, Nat. Phys. **7**, 907 (2011), arXiv: 1102.3256.
19 M. Hafezi, S. Mittal, J. Fan, A. Migdall, and J. M. Taylor, Nat. Photon. **7**, 1001 (2013), arXiv: 1302.2153.
20 Y. Plotnik, M. A. Bandres, S. Stützer, Y. Lumer, M. C. Rechtsman, A. Szameit, and M. Segev, Phys. Rev. B **94**, 020301 (2016).
21 D. D. Solnyshkov, A. V. Nalitov, and G. Malpuech, Phys. Rev. Lett. **116**, 046402 (2016), arXiv: 1506.04626.
22 P. St-Jean, V. Goblot, E. Galopin, A. Lemaître, T. Ozawa, L. Le Gratiet, I. Sagnes, J. Bloch, and A. Amo, Nat. Photon. **11**, 651 (2017), arXiv: 1704.07310.
23 M. A. Bandres, S. Wittek, G. Harari, M. Parto, J. Ren, M. Segev, D. N. Christodoulides, and M. Khajavikhan, Science **359**, eaar4005 (2018).
24 A. B. Khanikaev, S. Hossein Mousavi, W. K. Tse, M. Kargarian, A. H. MacDonald, and G. Shvets, Nat. Mater. **12**, 233 (2012), arXiv: 1204.5700.
25 W. J. Chen, S. J. Jiang, X. D. Chen, B. Zhu, L. Zhou, J. W. Dong, and C. T. Chan, Nat. Commun. **5**, 5782 (2014), arXiv: 1401.0367.
26 L. H. Wu, and X. Hu, Phys. Rev. Lett. **114**, 223901 (2015).
27 Y. Yang, Y. F. Xu, T. Xu, H. X. Wang, J. H. Jiang, X. Hu, and Z. H. Hang, Phys. Rev. Lett. **120**, 217401 (2018).
28 T. Ma, and G. Shvets, New J. Phys. **18**, 025012 (2016), arXiv: 1601.06673.
29 J. W. Dong, X. D. Chen, H. Zhu, Y. Wang, and X. Zhang, Nat. Mater. **16**, 298 (2017).
30 X. D. Chen, F. L. Zhao, M. Chen, and J. W. Dong, Phys. Rev. B **96**, 020202 (2017), arXiv: 1602.03352.
31 F. Gao, H. Xue, Z. Yang, K. Lai, Y. Yu, X. Lin, Y. Chong, G. Shvets, and B. Zhang, Nat. Phys. **14**, 140 (2018).
32 X. Wu, Y. Meng, J. Tian, Y. Huang, H. Xiang, D. Han, and W. Wen, Nat. Commun. **8**, 1304 (2017), arXiv: 1703.04570.
33 J. W. Liu, F. L. Shi, X. T. He, G. J. Tang, W. J. Chen, X. D. Chen, and J. W. Dong, Adv. Phys.-X **6**, 1905546 (2021).
34 H. Xue, Y. Yang, and B. Zhang, Adv. Photon. Res. **2**, 2100013 (2021).
35 Y. Yang, H. Jiang, and Z. H. Hang, Sci. Rep. **8**, 1588 (2018).
36 J. Noh, S. Huang, K. P. Chen, and M. C. Rechtsman, Phys. Rev. Lett. **120**, 063902 (2018), arXiv: 1706.00059.
37 D. Song, D. Leykam, J. Su, X. Liu, L. Tang, S. Liu, J. Zhao, N. K. Efremidis, J. Xu, and Z. Chen, Phys. Rev. Lett. **122**, 123903 (2019), arXiv: 1810.12736.
38 L. Ye, Y. Yang, Z. H. Hang, C. Qiu, and Z. Liu, Appl. Phys. Lett. **111**, 251107 (2017).
39 M. I. Shalaev, W. Walasik, A. Tsukernik, Y. Xu, and N. M. Litchinitser, Nat. Nanotech. **14**, 31 (2018).
40 X. T. He, E. T. Liang, J. J. Yuan, H. Y. Qiu, X. D. Chen, F. L. Zhao, and J. W. Dong, Nat. Commun. **10**, 872 (2019), arXiv: 1805.10962.
41 Y. Yang, Y. Yamagami, X. Yu, P. Pitchappa, J. Webber, B. Zhang, M. Fujita, T. Nagatsuma, and R. Singh, Nat. Photon. **14**, 446 (2020), arXiv: 1904.04213.
42 Y. Zeng, U. Chattopadhyay, B. Zhu, B. Qiang, J. Li, Y. Jin, L. Li, A. G. Davies, E. H. Linfield, B. Zhang, Y. Chong, and Q. J. Wang, Nature **578**, 246 (2020).
43 H. Yoshimi, T. Yamaguchi, R. Katsumi, Y. Ota, Y. Arakawa, and S. Iwamoto, Opt. Express **29**, 13441 (2021), arXiv: 2102.09252.
44 H. T. Phan, F. Liu, and K. Wakabayashi, Opt. Express **29**, 18277 (2021).
45 X. Xie, S. Yan, J. Dang, J. Yang, S. Xiao, Y. Wang, S. Shi, L. Yang, D. Dai, Y. Yuan, N. Luo, T. Cui, G. Chi, Z. Zuo, B. B. Li, C. Wang, and X. Xu, Phys. Rev. Appl. **16**, 014036 (2021), arXiv: 2106.13392.
46 L. Gu, Q. Yuan, Q. Zhao, Y. Ji, Z. Liu, L. Fang, X. Gan, and J. Zhao, J. Lightwave Technol. **39**, 5069 (2021), arXiv: 2105.07171.
47 A. M. Dubrovkin, U. Chattopadhyay, B. Qiang, O. Buchnev, Q. J. Wang, Y. Chong, and N. I. Zheludev, Appl. Phys. Lett. **116**, 191105 (2020).
48 H. Zhong, S. Xia, Y. Zhang, Y. Li, D. Song, C. Liu, and Z. Chen, Adv. Photon. **3**, 056001 (2021), arXiv: 2010.02902.
49 M. Qiu, and S. He, Phys. Lett. A **266**, 425 (2000).
50 E. Degirmenci, and P. Landais, Appl. Opt. **52**, 7367 (2013).
51 K. Wang, Phys. Rev. B **100**, 115140 (2019).
52 U. Kuhl, S. Barkhofen, T. Tudorovskiy, H. J. Stöckmann, T. Hossain, L. de Forges de Parny, and F. Mortessagne, Phys. Rev. B **82**, 094308 (2010), arXiv: 1006.0901.
53 J. Lu, C. Qiu, S. Xu, Y. Ye, M. Ke, and Z. Liu, Phys. Rev. B **89**, 134302 (2014).
54 S. Y. Yu, X. C. Sun, X. Ni, Q. Wang, X. J. Yan, C. He, X. P. Liu, L. Feng, M. H. Lu, and Y. F. Chen, Nat. Mater. **15**, 1243 (2016).
55 J. Lu, C. Qiu, M. Ke, and Z. Liu, Phys. Rev. Lett. **116**, 093901 (2016), arXiv: 1707.02059.
56 X. D. Chen, X. T. He, and J. W. Dong, Laser Photon. Rev. **13**, 1900091 (2019).
57 L. He, H. Zhang, W. Zhang, Y. Wang, and X. Zhang, New J. Phys. **23**, 093026 (2021).
58 B. Xie, G. Su, H. F. Wang, F. Liu, L. Hu, S. Y. Yu, P. Zhan, M. H. Lu, Z. Wang, and Y. F. Chen, Nat. Commun. **11**, 3768 (2020).
59 M. Jung, R. G. Gladstone, and G. B. Shvets, Adv. Photon. **2**, 046003 (2020).
60 T. Ma, A. B. Khanikaev, S. H. Mousavi, and G. Shvets, Phys. Rev. Lett. **114**, 127401 (2015).
61 X. D. Chen, W. M. Deng, F. L. Zhao, and J. W. Dong, Laser Photon. Rev. **12**, 1800073 (2018).